

# Functional and diffusion MRI reveal the functional and structural basis of infants' noxious-evoked brain activity

**Luke Baxter**

Department of Paediatrics, University of Oxford, UK <https://orcid.org/0000-0001-9548-7162>

**Fiona Moultrie**

Department of Paediatrics, University of Oxford, UK

**Sean Fitzgibbon**

FMRIB, Wellcome Centre for Integrative Neuroimaging, University of Oxford, UK

**Marianne Aspbury**

Department of Paediatrics, University of Oxford, UK

**Roshni Mansfield**

Department of Paediatrics, University of Oxford, UK

**Matteo Bastiani**

FMRIB, Wellcome Centre for Integrative Neuroimaging, University of Oxford, UK

**Richard Rogers**

Nuffield Department of Anaesthetics, John Radcliffe Hospital, Oxford, UK

**Saad Jbabdi**

FMRIB, Wellcome Centre for Integrative Neuroimaging, University of Oxford, UK

**Eugene Duff**

Department of Paediatrics, University of Oxford, UK

**Rebecca Slater** (✉ [rebecca.slater@paediatrics.ox.ac.uk](mailto:rebecca.slater@paediatrics.ox.ac.uk))

Department of Paediatrics, University of Oxford, UK

---

## Research Article

**Keywords:** Infant, pain, noxious, MRI, resting state, diffusion, prediction, individual variability, dHCP

**Posted Date:** February 18th, 2021

**DOI:** <https://doi.org/10.21203/rs.3.rs-25860/v2>

**License:**   This work is licensed under a Creative Commons Attribution 4.0 International License.

[Read Full License](#)

**Version of Record:** A version of this preprint was published on May 12th, 2021. See the published version at <https://doi.org/10.1038/s41467-021-22960-0>.

# Abstract

Understanding the neurophysiology underlying neonatal responses to noxious stimulation is central to improving early life pain management. In this neonatal multimodal MRI study, we use resting-state and diffusion MRI to investigate inter-individual variability in noxious-evoked brain activity. We demonstrate that cerebral haemodynamic responses to experimental noxious stimulation can be predicted from separately acquired resting-state brain activity (n=18). Applying this prediction model to independent Developing Human Connectome Project data (n=215), we identify negative associations between predicted noxious-evoked responses and white matter mean diffusivity. These associations are subsequently confirmed in the original noxious stimulation paradigm dataset, validating the prediction model. This study in healthy neonates demonstrates that noxious-evoked brain activity is tightly coupled to both resting-state activity and white matter microstructure, that neural features can be used to predict responses to noxious stimulation, and that the dHCP dataset could be utilised for future exploratory research of early life pain system neurophysiology.

## Introduction

Neonates routinely undergo numerous painful procedures as part of standard clinical care shortly after birth during their stay in hospital<sup>1</sup>. Their lack of verbal communication, brief extra-uterine medical history, and ambiguity in behavioural and physiological responses that underpin infant pain scales<sup>2</sup>, lead to a high degree of uncertainty in clinical decision-making related to treatment of neonatal pain. Understanding and anticipating an individual newborn's response to noxious input would advance efforts of personalised pre-emptive pain minimisation in this vulnerable population.

In experimental settings, a multitude of complementary behavioural, physiological, and neural measures are used in an attempt to quantify neonatal pain, with a high degree of individual variability observed within all modalities<sup>3-6</sup>. Due to the neural origin of pain<sup>3</sup> and the recent feasibility of collecting multiple high-quality MRI imaging modalities of the neonatal brain within a single scan session, we used a multimodal MRI approach to investigate the neurophysiological basis for individual variability in neonates' blood oxygen level dependent (BOLD) responses to noxious stimulation. Our noxious stimulation paradigm involved applying a mild experimental sharp-touch stimulus (PinPrick Stimulator, MRC Systems) to the neonate's foot, evoking brain activity known to be similarly evoked by a range of tissue-damaging medical procedures, such as blood sampling, vaccinations, and cannulations<sup>3,7,8</sup>. The pinprick stimulus produces responses of lower amplitude than those of clinical procedures and does not cause behavioural distress<sup>3</sup>, but activates A-fibre nociceptors in the periphery<sup>9</sup> and elicits noxious-evoked brain activity in the cerebral cortex<sup>10-13</sup>, making it a useful experimental tool to better understand neonatal pain processing.

Due to the emergent and multifaceted nature of pain<sup>14,15</sup>, we focus on assessing the overall BOLD response amplitude. While this BOLD response neither directly reflects nociception, the neural process of

encoding noxious stimuli<sup>16</sup>, nor pain perception, the unpleasant sensory and emotional subjective experience<sup>16</sup>, it is a pertinent and accessible feature of central importance to understanding neonates' neural responses to noxious input and the neurophysiology of the early developing pain system. This overall noxious-evoked BOLD response pattern resembles that of adults<sup>10</sup> and expresses the adult Neurologic Pain Signature (NPS)<sup>17</sup>, a multivariate fMRI signature predictive of adult verbal reports of physical pain. The overall response captures inter-individual variability in the multidimensional noxious-evoked activity, which is tightly linked to the pre-stimulation functional status of the descending pain modulatory system<sup>18</sup> and is likely to be driven by variability in sensory-discriminative, cognitive, and emotional aspects.

Furthermore, a holistic multidimensional noxious-evoked brain response metric reflects and should facilitate future harmonisation with existing validated multidimensional infant clinical pain assessment tools, such as the widely used PIPP-R scale (Premature Infant Pain Profile Revised)<sup>19-21</sup>, which integrates across multiple pain-relevant behavioural and autonomic response features to provide a reliable overall measure of this complex phenomenon<sup>22</sup>. Due to the subjective nature of pain and non-verbal nature of neonates, having to rely on objectively measured noxious-evoked response features for infant pain measurement is a major challenge for the field of infant pain research, and thus facilitating this cross-modality integration is vital for mitigating limitations of each individual objective assessment approach<sup>23,24</sup>. We augment the analysis of overall BOLD responses with a parallel study of the expression in this data of Neurosynth-derived templates<sup>25</sup> and adult pain signatures, providing insight into the processes contributing to the observed responses.

To better understand the neurophysiological basis for individual variability in neonates' overall BOLD responses to noxious stimulation, we test whether noxious-evoked responses can be predicted from nociception-free resting-state brain activity. To determine whether response amplitudes reflect the current state of the infant, or a developmental trait effect, we further test whether responses are associated with underlying white matter microstructure. We mitigate the small sample sizes limitation inherent to neonatal fMRI pain studies by identifying consistent findings in a large independent age-matched sample from the Developing Human Connectome Project (dHCP) dataset (<http://www.developingconnectome.org>).

A high degree of correspondence between resting-state and task-related brain activities has been observed in adult fMRI studies<sup>26,27</sup>. In adults, fMRI-recorded resting-state activity is a distinguishing feature of an individual's brain functionality<sup>28</sup>, predicts individuals' task-related brain activity under both experimental<sup>29</sup> and clinical conditions<sup>30</sup>, as well as adults' individual pain sensitivities<sup>31</sup>. While analogous studies have not been conducted in neonatal populations, large-scale resting-state networks are detectable using fMRI from birth and correspond to adult canonical resting-state and task-response networks<sup>32,33</sup>, suggesting a similar functional coupling could exist at this early developmental stage.

Previous studies have demonstrated sensitivity of neonates' noxious-evoked cerebral activity to sleep state<sup>13</sup> and physiological stress<sup>34</sup>. To disambiguate temporally stable trait effects from transient state effects, which are arguably of higher relevance for clinical pre-emptive decision making, we assess associations between neonates' noxious-evoked response amplitudes and underlying white matter microstructure using diffusion MRI (dMRI) data. These microstructural features reflect the integrity of developing structural connectivity, constraining noxious-evoked responses. Temporal stability was assessed through association with microstructure rather than looking at stability across multiple test occasions, as neonates could only be tested on a single occasion.

Due to the large number of potential white matter features that could be studied and the lack of neonatal research into associations between noxious-evoked activity and white matter microstructure that could guide the feature selection process, we adopted a two-part two-dataset approach, involving exploration of a range of structure-function associations in the dHCP dataset to formulate data-driven hypotheses, followed by independent confirmation of these hypotheses in our noxious stimulation paradigm dataset. We use the dHCP dataset to explore possible structure-function relationships due to its larger sample size and thus greater statistical power. Given that the dHCP dataset does not include noxious stimulation paradigm data, we generate a predicted noxious-evoked response amplitude per neonate from their resting-state data using the prediction model originally trained in our local noxious stimulation paradigm dataset. We focus on 16 white matter tracts previously used in a recent dHCP dMRI publication<sup>35</sup> and three tensor model parameters generated by the dHCP dMRI preprocessing pipeline<sup>35</sup>: mean diffusivity, fractional anisotropy, and mean kurtosis. Structure-function associations identified in this exploratory analysis were subsequently tested in our noxious stimulation paradigm dataset, for which measured noxious-evoked response amplitudes are available.

This work provides novel insight into the neurophysiological basis for normative variability in cerebral responses to noxious input in healthy neonates. We demonstrate a pain-relevant neural structure-function relationship, and the observed tight coupling between resting-state and noxious-evoked response activities provides proof-of-concept that neonates' nociception-free resting-state brain activity can be used to predict their brain response to noxious stimulation.

## Results

### **Neonates displayed wide variability in haemodynamic response amplitude to noxious stimulation**

We quantified the change in brain activity evoked by a 128 mN pinprick experimental noxious stimulus to the foot in 18 healthy neonates (Figure 1). The noxious-evoked response was localised to functional brain regions classically considered part of the adult nociceptive pain system, including pre- and post-central gyri, opercular and insular cortices, and the thalamus<sup>36</sup> (Figure 2a). Responses were highly variable between subjects including positive, negligible, and negative BOLD responses (Figure 1 heat maps). Summarising each neonate's noxious-evoked response map relative to the group average response map, response amplitudes ranged from -0.87 to 5.60 (Figure 1 scalar values).

For each neonate, the noxious-evoked response was well fit by the term-neonate double gamma haemodynamic response function (HRF). There were no obvious signs of gross artefactual errors such as head motion-related spikes (Supplementary Figure 1) and no association with variable response latencies assessed by HRF goodness-of-fit (Supplementary Figure 3), suggesting that the estimated noxious-evoked activity reflects physiologically meaningful cerebral BOLD responses to noxious input.

To gain insight into processes underlying the observed noxious-evoked activity, we assessed expression of two template maps that have been independently linked to pain in adults. Both the Neurosynth<sup>25</sup> pain association test map (<https://www.neurosynth.org/analyses/terms/pain>), derived from a search of a meta-analytic database of fMRI study activation co-ordinates for the keyword “pain”, and the adult Neurologic Pain Signature (NPS)<sup>37</sup>, which predicts variations in adult verbal reports of pain intensity, were significantly expressed (Figure 2bi and Table 1 T-test results). We also assessed expression of a number of related and control templates. As negative controls, we assessed the Neurosynth “visual” pattern as well as the adult social rejection pain signature<sup>37</sup>, and found neither to be expressed. Of the sensory, cognitive, and emotional Neurosynth patterns assessed, only the “nociceptive” pattern was significantly expressed, while patterns for “attention”, “unpleasant”, “salience”, and “arousal” were not (Figure 2bi and Table 1 T-test results).

In addition to group average template expression, we assessed associations between the inter-individual variability in overall noxious-evoked response amplitudes (regression coefficients) and the correspondence between neonates’ noxious-evoked response maps and each template (correlation coefficients). Of the nine adult templates assessed, significant associations were only observed between noxious-evoked response amplitudes and adult template expression for NPS and Neurosynth Pain and Nociceptive templates (Figure 2ii-iii and Table 1 Correlation results). Thus, the larger the overall BOLD response amplitude to noxious stimulation, the closer the correspondence with adult pain and nociceptive signatures. Correlation results for all templates are presented in Supplementary Figure 9 and Table 1. Collectively, these adult template results support the interpretation that the neonates’ overall noxious-evoked responses are pain-relevant signals.

### **Nine resting-state networks were replicable across the noxious stimulation paradigm and dHCP datasets**

In the same cohort (n=18), nine resting-state networks were robustly identified from separate resting-state scans using probabilistic functional mode (PFM) analysis (Figure 3). These included six sensory and motor networks (two visual, two auditory, and two somatomotor networks) and three cognitive networks (default mode, dorsal attention, and executive control networks). To consider a network robust and suitable for inclusion in subsequent analyses, networks needed to be replicable across both the noxious stimulation paradigm dataset (n=18) and an independent age-matched dHCP dataset (n=242) previously analysed using PFM<sup>38</sup>. Eleven non-zero modes of variation were identified in the noxious stimulation paradigm dataset, nine of which corresponded to networks in the dHCP dataset, assessed using spatial correlation followed by visual confirmation (Figure 3). Matched networks were highly consistent between

datasets with spatial correlations between unthresholded maps ranging from 0.62 to 0.89 (mean=0.77) (Figure 3 scalar values).

In our local dataset, resting-state network amplitudes were quantified using multiple regression of the nine dHCP networks (Figure 3 bottom row) onto each neonate's resting-state data, and each resulting network timeseries summarised as an amplitude using median absolute deviation (MAD), which ensures robustness to outliers. Examining network timeseries, there were no obvious signs of gross artefactual errors (Supplementary Figure 2). While network timeseries outliers existed, they have minimal influence on amplitudes estimated using MAD. Finally, no association existed between neonates' resting-state network timeseries outlier content and noxious-evoked response amplitudes (Supplementary Figure 3), suggesting that individual variability in response amplitudes was not associated with individual variability in resting-state network timeseries quality.

### **Resting-state network amplitudes predicted noxious-evoked response amplitudes**

We predicted neonates' overall noxious-evoked response amplitudes (Figure 1 scalar values) from their nociception-free resting-state network amplitudes with statistically significant accuracy ( $R^2=0.62$ ,  $p=0.003$ ) (Figure 4; Table 2). Resting-state network amplitudes were also predictive of both the Neurosynth ( $R^2=0.46$ ,  $p=0.006$ ) and NPS ( $R^2=0.42$ ,  $p=0.013$ ) response magnitudes (Table 2). Using a linear support vector regression (SVR) model, predictions were generated using leave-one-out cross-validation, including cross-validated adjustment for several confounds (see Methods).

Three resting-state imaging confounds (head motion, cerebrospinal fluid and white matter amplitudes), were additionally tested in a multivariate model but were not predictive of the neonates' noxious-evoked response amplitudes (Figure 4; Table 2). Similarly, six non-fMRI clinical variables, which included postmenstrual age (PMA), gestational age (GA), postnatal age (PNA), birth weight, total brain volume (TBV), and sex, were tested in a multivariate model and were also not predictive (Figure 4; Table 2). The lack of association between noxious-evoked response amplitudes and resting-state imaging confounds suggest that the predictive value of resting-state network amplitudes was not mediated by undesirable confounding features of resting-state data, but rather by the correspondence between resting-state and noxious-evoked brain activities. These brain function similarities could not be explained by the biologically interesting variables of age, birth weight, brain volume, or sex.

Examining the correlation polarity of each network individually, eight of nine networks were positively correlated with noxious-evoked response amplitudes, with the single negative correlation being negligible (executive control network,  $r=-0.03$ ) (Supplementary Figure 4a). Examining the predictive value of each network individually, only the SMN exhibit notable predictive value, with a prediction performance ( $R^2=0.60$ ) comparable to our multivariate prediction model performance ( $R^2=0.62$ ) (Supplementary Figure 4b). This suggests a near-global positive association between resting-state network amplitudes and noxious-evoked response amplitudes, with meaningful network-to-network variability in association strength such that the most robust functional coupling was with the functionally relevant SMN. These

univariate correlation and prediction analyses did not reveal any individual resting-state imaging confound or clinical variable to have a strong association with noxious-evoked response amplitudes (Supplementary Figure 4).

### **Noxious-evoked response amplitudes were significantly negatively associated with white matter mean diffusivity**

The SVR prediction model was trained on neonates in the noxious stimulation paradigm dataset (n=18) to map from confound-adjusted resting-state network amplitudes to confound-adjusted noxious-evoked response amplitudes. Using this model, predicted noxious-evoked response amplitudes were generated for an age-matched dHCP sample (n=215) for which both resting-state and diffusion data were available. These predicted noxious-evoked response amplitudes were used for the structure-function exploratory arm analyses due to the large sample size, and the results formed the basis for data-driven hypotheses regarding noxious stimulation-related structure-function associations. These hypotheses were subsequently tested in the structure-function confirmatory arm analyses using the local noxious stimulation paradigm dataset, for which measured noxious-evoked response amplitudes were available.

#### *Exploratory arm:*

We assessed mean diffusivity (MD), fractional anisotropy (FA), and mean kurtosis (MK) across 16 bilateral white matter tracts<sup>35</sup>. Of the 48 univariate correlations tested (16 tracts x 3 parameters), the predicted noxious-evoked response amplitudes were significantly negatively correlated with MD in five white matter tracts: anterior and superior thalamic radiation, corticospinal tract, forceps minor, and uncinate fasciculus (Figure 5). Negative associations with MD and positive associations with FA existed for all tracts. However, we limited our data-driven hypotheses to the MD of these five specific tracts, because they were the most robust subset of structure-function associations, and in addition to global effects, we expect some specificity to certain functionally relevant tracts.

Due to the consistent negative correlation polarity, the variance of these five tracts was pooled using principal component analysis (PCA). The first principal component of MD across these five tracts (MD PC1) accounted for 83.6% of cross-subject variance, and as expected, was negatively correlated with the predicted noxious-evoked response amplitudes:  $r = -0.25$ ,  $p = 0.0001$  (this statistical test is biased due to circularity in explanatory variable selection<sup>39</sup>, but the bias is restricted to the exploratory arm) (Figure 6a). These significant negative correlations between noxious-evoked response amplitudes and MD formed the basis for two testable hypotheses: (i) the coefficient polarities for correlations between noxious-evoked response amplitudes and MD are negative for each of these five tracts, and (ii) MD PC1 across these five tracts is significantly negatively correlated with noxious-evoked response amplitudes.

#### *Confirmatory arm:*

To validate these exploratory findings and the resting-state prediction model underpinning them, we tested whether measured noxious-evoked brain activity in the noxious stimulation paradigm dataset

(n=17) was also dependent on the same structural brain properties. For each of the five white matter tracts, MD was negatively correlated with noxious-evoked response amplitudes (Figure 6b). Additionally, MD PC1 accounted for 88.82% of between-subject variance and was significantly negatively correlated with neonates' noxious-evoked response amplitudes:  $r=-0.454$ ,  $p=0.034$  (Figure 6b). Thus, within our noxious stimulation paradigm dataset, over 20% of between-subject variation in noxious-evoked response amplitudes could be explained by the MD of these five functionally relevant white matter tracts.

We also observed widespread negative associations with MD and positive association with FA (Supplementary Figure 6a), reproducing the global structure-function association effects observed in the dHCP dataset (Figure 5). Additionally, there was noticeable tract-to-tract variability in association strength in both datasets. Comparing this tract-to-tract variability between datasets, high similarity was observed for MD ( $r=0.62$ ) (Supplementary Figure 6b), suggesting that tracts with strongest associations between MD and noxious-evoked response amplitudes were relatively consistent between datasets. We compared the variance in noxious-evoked response amplitudes explained by MD PC1 of these five specific tracts to that of the global signal (MD PC1 across all 16 tracts) as well as to all possible combinations of the 16 tracts (Supplementary Figure 7). The specific 5-tract MD PC1  $r^2=0.21$  outperformed the global 16-tract MD PC1  $r^2=0.17$ , and featured in the 92.3<sup>th</sup> percentile of the distribution of all possible tract combinations.

These results suggest global structure-function associations exist between noxious-evoked response amplitudes and white matter MD and FA. Meaningful tract-to-tract variability in MD association was reproducible between datasets, such that a subset of pain-relevant tracts exhibited greater explanatory value than a global MD metric, which does not account for tract-to-tract variability in functional relevance.

## Discussion

### **Neonates displayed wide variability in haemodynamic response amplitude to noxious stimulation**

We quantified the change in brain activity evoked by a 128 mN pinprick experimental noxious stimulus to the foot in 18 healthy neonates (Figure 1). The noxious-evoked response was localised to functional brain regions classically considered part of the adult nociceptive pain system, including pre- and post-central gyri, opercular and insular cortices, and the thalamus<sup>36</sup> (Figure 2a). Responses were highly variable between subjects including positive, negligible, and negative BOLD responses (Figure 1 heat maps). Summarising each neonate's noxious-evoked response map relative to the group average response map, response amplitudes ranged from -0.87 to 5.60 (Figure 1 scalar values).

For each neonate, the noxious-evoked response was well fit by the term-neonate double gamma haemodynamic response function (HRF). There were no obvious signs of gross artefactual errors such as head motion-related spikes (Supplementary Figure 1) and no association with variable response latencies assessed by HRF goodness-of-fit (Supplementary Figure 3), suggesting that the estimated noxious-evoked activity reflects physiologically meaningful cerebral BOLD responses to noxious input.

To gain insight into processes underlying the observed noxious-evoked activity, we assessed expression of two template maps that have been independently linked to pain in adults. Both the Neurosynth<sup>25</sup> pain association test map (<https://www.neurosynth.org/analyses/terms/pain>), derived from a search of a meta-analytic database of fMRI study activation co-ordinates for the keyword “pain”, and the adult Neurologic Pain Signature (NPS)<sup>37</sup>, which predicts variations in adult verbal reports of pain intensity, were significantly expressed (Figure 2bi and Table 1 T-test results). We also assessed expression of a number of related and control templates. As negative controls, we assessed the Neurosynth “visual” pattern as well as the adult social rejection pain signature<sup>37</sup>, and found neither to be expressed. Of the sensory, cognitive, and emotional Neurosynth patterns assessed, only the “nociceptive” pattern was significantly expressed, while patterns for “attention”, “unpleasant”, “salience”, and “arousal” were not (Figure 2bi and Table 1 T-test results).

In addition to group average template expression, we assessed associations between the inter-individual variability in overall noxious-evoked response amplitudes (regression coefficients) and the correspondence between neonates’ noxious-evoked response maps and each template (correlation coefficients). Of the nine adult templates assessed, significant associations were only observed between noxious-evoked response amplitudes and adult template expression for NPS and Neurosynth Pain and Nociceptive templates (Figure 2ii-iii and Table 1 Correlation results). Thus, the larger the overall BOLD response amplitude to noxious stimulation, the closer the correspondence with adult pain and nociceptive signatures. Correlation results for all templates are presented in Supplementary Figure 9 and Table 1. Collectively, these adult template results support the interpretation that the neonates’ overall noxious-evoked responses are pain-relevant signals.

### **Nine resting-state networks were replicable across the noxious stimulation paradigm and dHCP datasets**

In the same cohort (n=18), nine resting-state networks were robustly identified from separate resting-state scans using probabilistic functional mode (PFM) analysis (Figure 3). These included six sensory and motor networks (two visual, two auditory, and two somatomotor networks) and three cognitive networks (default mode, dorsal attention, and executive control networks). To consider a network robust and suitable for inclusion in subsequent analyses, networks needed to be replicable across both the noxious stimulation paradigm dataset (n=18) and an independent age-matched dHCP dataset (n=242) previously analysed using PFM<sup>38</sup>. Eleven non-zero modes of variation were identified in the noxious stimulation paradigm dataset, nine of which corresponded to networks in the dHCP dataset, assessed using spatial correlation followed by visual confirmation (Figure 3). Matched networks were highly consistent between datasets with spatial correlations between unthresholded maps ranging from 0.62 to 0.89 (mean=0.77) (Figure 3 scalar values).

In our local dataset, resting-state network amplitudes were quantified using multiple regression of the nine dHCP networks (Figure 3 bottom row) onto each neonate’s resting-state data, and each resulting network timeseries summarised as an amplitude using median absolute deviation (MAD), which ensures robustness to outliers. Examining network timeseries, there were no obvious signs of gross artefactual

errors (Supplementary Figure 2). While network timeseries outliers existed, they have minimal influence on amplitudes estimated using MAD. Finally, no association existed between neonates' resting-state network timeseries outlier content and noxious-evoked response amplitudes (Supplementary Figure 3), suggesting that individual variability in response amplitudes was not associated with individual variability in resting-state network timeseries quality.

### **Resting-state network amplitudes predicted noxious-evoked response amplitudes**

We predicted neonates' overall noxious-evoked response amplitudes (Figure 1 scalar values) from their nociception-free resting-state network amplitudes with statistically significant accuracy ( $R^2=0.62$ ,  $p=0.003$ ) (Figure 4; Table 2). Resting-state network amplitudes were also predictive of both the Neurosynth ( $R^2=0.46$ ,  $p=0.006$ ) and NPS ( $R^2=0.42$ ,  $p=0.013$ ) response magnitudes (Table 2). Using a linear support vector regression (SVR) model, predictions were generated using leave-one-out cross-validation, including cross-validated adjustment for several confounds (see Methods).

Three resting-state imaging confounds (head motion, cerebrospinal fluid and white matter amplitudes), were additionally tested in a multivariate model but were not predictive of the neonates' noxious-evoked response amplitudes (Figure 4; Table 2). Similarly, six non-fMRI clinical variables, which included postmenstrual age (PMA), gestational age (GA), postnatal age (PNA), birth weight, total brain volume (TBV), and sex, were tested in a multivariate model and were also not predictive (Figure 4; Table 2). The lack of association between noxious-evoked response amplitudes and resting-state imaging confounds suggest that the predictive value of resting-state network amplitudes was not mediated by undesirable confounding features of resting-state data, but rather by the correspondence between resting-state and noxious-evoked brain activities. These brain function similarities could not be explained by the biologically interesting variables of age, birth weight, brain volume, or sex.

Examining the correlation polarity of each network individually, eight of nine networks were positively correlated with noxious-evoked response amplitudes, with the single negative correlation being negligible (executive control network,  $r=-0.03$ ) (Supplementary Figure 4a). Examining the predictive value of each network individually, only the SMN exhibit notable predictive value, with a prediction performance ( $R^2=0.60$ ) comparable to our multivariate prediction model performance ( $R^2=0.62$ ) (Supplementary Figure 4b). This suggests a near-global positive association between resting-state network amplitudes and noxious-evoked response amplitudes, with meaningful network-to-network variability in association strength such that the most robust functional coupling was with the functionally relevant SMN. These univariate correlation and prediction analyses did not reveal any individual resting-state imaging confound or clinical variable to have a strong association with noxious-evoked response amplitudes (Supplementary Figure 4).

### **Noxious-evoked response amplitudes were significantly negatively associated with white matter mean diffusivity**

The SVR prediction model was trained on neonates in the noxious stimulation paradigm dataset (n=18) to map from confound-adjusted resting-state network amplitudes to confound-adjusted noxious-evoked response amplitudes. Using this model, predicted noxious-evoked response amplitudes were generated for an age-matched dHCP sample (n=215) for which both resting-state and diffusion data were available. These predicted noxious-evoked response amplitudes were used for the structure-function exploratory arm analyses due to the large sample size, and the results formed the basis for data-driven hypotheses regarding noxious stimulation-related structure-function associations. These hypotheses were subsequently tested in the structure-function confirmatory arm analyses using the local noxious stimulation paradigm dataset, for which measured noxious-evoked response amplitudes were available.

#### *Exploratory arm:*

We assessed mean diffusivity (MD), fractional anisotropy (FA), and mean kurtosis (MK) across 16 bilateral white matter tracts<sup>35</sup>. Of the 48 univariate correlations tested (16 tracts x 3 parameters), the predicted noxious-evoked response amplitudes were significantly negatively correlated with MD in five white matter tracts: anterior and superior thalamic radiation, corticospinal tract, forceps minor, and uncinate fasciculus (Figure 5). Negative associations with MD and positive associations with FA existed for all tracts. However, we limited our data-driven hypotheses to the MD of these five specific tracts, because they were the most robust subset of structure-function associations, and in addition to global effects, we expect some specificity to certain functionally relevant tracts.

Due to the consistent negative correlation polarity, the variance of these five tracts was pooled using principal component analysis (PCA). The first principal component of MD across these five tracts (MD PC1) accounted for 83.6% of cross-subject variance, and as expected, was negatively correlated with the predicted noxious-evoked response amplitudes:  $r = -0.25$ ,  $p = 0.0001$  (this statistical test is biased due to circularity in explanatory variable selection<sup>39</sup>, but the bias is restricted to the exploratory arm) (Figure 6a). These significant negative correlations between noxious-evoked response amplitudes and MD formed the basis for two testable hypotheses: (i) the coefficient polarities for correlations between noxious-evoked response amplitudes and MD are negative for each of these five tracts, and (ii) MD PC1 across these five tracts is significantly negatively correlated with noxious-evoked response amplitudes.

#### *Confirmatory arm:*

To validate these exploratory findings and the resting-state prediction model underpinning them, we tested whether measured noxious-evoked brain activity in the noxious stimulation paradigm dataset (n=17) was also dependent on the same structural brain properties. For each of the five white matter tracts, MD was negatively correlated with noxious-evoked response amplitudes (Figure 6b). Additionally, MD PC1 accounted for 88.82% of between-subject variance and was significantly negatively correlated with neonates' noxious-evoked response amplitudes:  $r = -0.454$ ,  $p = 0.034$  (Figure 6b). Thus, within our noxious stimulation paradigm dataset, over 20% of between-subject variation in noxious-evoked response amplitudes could be explained by the MD of these five functionally relevant white matter tracts.

We also observed widespread negative associations with MD and positive association with FA (Supplementary Figure 6a), reproducing the global structure-function association effects observed in the dHCP dataset (Figure 5). Additionally, there was noticeable tract-to-tract variability in association strength in both datasets. Comparing this tract-to-tract variability between datasets, high similarity was observed for MD ( $r=0.62$ ) (Supplementary Figure 6b), suggesting that tracts with strongest associations between MD and noxious-evoked response amplitudes were relatively consistent between datasets. We compared the variance in noxious-evoked response amplitudes explained by MD PC1 of these five specific tracts to that of the global signal (MD PC1 across all 16 tracts) as well as to all possible combinations of the 16 tracts (Supplementary Figure 7). The specific 5-tract MD PC1  $r^2=0.21$  outperformed the global 16-tract MD PC1  $r^2=0.17$ , and featured in the 92.3<sup>th</sup> percentile of the distribution of all possible tract combinations.

These results suggest global structure-function associations exist between noxious-evoked response amplitudes and white matter MD and FA. Meaningful tract-to-tract variability in MD association was reproducible between datasets, such that a subset of pain-relevant tracts exhibited greater explanatory value than a global MD metric, which does not account for tract-to-tract variability in functional relevance.

## Methods

### Part 1: Relating noxious-evoked response amplitude to resting-state activity

#### Subject information

We recruited healthy neonates from the John Radcliffe Hospital postnatal ward (Oxford University Hospital NHS Trust). Neonates were considered healthy if they were inpatients that never required admission to the neonatal unit, had no history of congenital conditions or neurological problems, and were clinically stable at time of study. Written informed consent was obtained from parents prior to the study. Ethical approval was obtained from an NHS Research Ethics Committee (National Research Ethics Service, REC reference: 12/SC/0447), and research was conducted in accordance with Good Clinical Practice guidelines and the Declaration of Helsinki.

Twenty one neonates had noxious-evoked and resting-state data collected. Subjects were excluded from analysis if (i) either scan session was not fully completed, in order to remove inter-subject variability in data quality related to scan length, and (ii) the vertex of the cerebral cortex left the scan field of view for more than 5% of the scan session, in order to ensure reliable data in this functionally relevant brain region. Using these criteria, three subjects were excluded resulting in a final sample of  $n=18$  neonates. Demographic details for this sample are displayed in Table 3.

#### Experimental design

Scans occurred in the Wellcome Centre for Integrative Neuroimaging (Oxford, UK). Neonates were fed and swaddled, fitted with ear protection, then placed on a vacuum-positioning mattress with padding around

the head. Heart rate and blood oxygen saturation were monitored throughout scanning, but were not of sufficient quality for analysis. The noxious stimulation paradigm was an event-related design in which a mild non-skin-breaking noxious stimulus, the 128 mN sharp-touch pinprick (PinPrick Stimulator, MRC Systems), was applied to the dorsum of the left foot: ten trials, 1 s per trial, 25 s minimum inter-stimulus interval<sup>10</sup>. Stimuli were applied only when the neonates were naturally still to minimise the influence of motion artefacts. For all other scan types, neonates lay passively in the scanner. No sedatives were used at any stage.

## **MRI data acquisition**

All data were collected on a 3T Siemens Prisma with an adult 32-channel receive coil using the following scan parameters. Structural: T2-weighted, TSE (factor 11), 150° flip angle, TE=89 ms, TR=14,740 ms, GRAPPA 3, 192 × 192 in-plane matrix size, 126 slices, 1 mm isotropic voxels, acquisition time (TA)=2 mins 13 s. Fieldmap: gradient echo, 2DFT readout, dual echo TE1/TE2=4.92/7.38 ms, TR=550 ms, 46° flip angle, 90 × 90 in-plane matrix size, 56 slices, 2 mm isotropic voxels, TA=1 min 40 s. Resting-state and noxious stimulation fMRI: T2\* BOLD-weighted, gradient echo, EPI readout, 70° flip angle, TE=50 ms<sup>64</sup>, TR=1,300 ms, multiband 4<sup>65,66</sup>, 90 × 90 in-plane matrix size, 56 slices, 2 mm isotropic voxels, AP phase encode direction. Resting-state TA=10 mins 50 s (500 volumes), mean noxious stimulation TA=6 min approx. (277 volumes approx.). Diffusion MRI: T2 diffusion-weighted, spin echo, EPI readout, 90° flip angle, TE=73 ms, TR=2,900 ms, multiband 3, 102 × 102 in-plane matrix size, 60 slices, 1.75 mm isotropic voxels, AP phase encode direction, multishell (b=500, 1000, 2000 s/mm<sup>2</sup>), 143 directions uniformly distributed over the whole sphere, TA=8 mins. Phase-reversed b0 images were collected to derive a spin-echo fieldmap for distortion correction of the diffusion data. The entire MRI acquisition protocol had a nominal duration of 40 mins.

## **MRI data preprocessing**

All MRI data were preprocessed using Developing Human Connectome Project (dHCP) pipelines. The T2 structural data were processed using the MIRTk Draw-EM neonatal pipeline<sup>67,68</sup>. Noxious stimulation and resting-state fMRI data were preprocessed using the dHCP fMRI pipeline<sup>47,69</sup>. Data were motion and distortion corrected using FSL's EDDY<sup>70,71</sup>, which included slice-to-volume motion correction<sup>72</sup> and susceptibility-by-movement distortion correction<sup>73</sup>. Noxious stimulation data were high-pass temporally filtered at 0.01 Hz, and resting-state data at 0.005 Hz. Data were denoised using FSL's FIX<sup>74,75</sup>, low-pass spatially filtered with a 3 mm FWHM filter using FSL's SUSAN<sup>76</sup>, and scaled to a common global spatiotemporal median. For spatial normalisation, data were registered from functional to structural space using BBR<sup>77</sup> with FSL's FLIRT<sup>78,79</sup>, then from structural space to the 40-week standard template<sup>80</sup> using ANTs's SyN<sup>81</sup>.

Diffusion data were analysed using the dHCP dMRI pipeline<sup>35,82</sup>. Phase-reversed fieldmaps were processed using FSL's TOPUP<sup>83,84</sup>. Data were corrected for motion, distortion, and eddy currents using

FSL's EDDY, which included outlier detection and replacement<sup>85</sup>, slice-to-volume motion correction, and susceptibility-by-movement distortion correction. Spatial normalisation followed the same sequence of registrations as the functional data.

### **Noxious-evoked response amplitudes**

Noxious-evoked response maps were generated using subject-level voxelwise GLM analysis in FSL's FEAT<sup>86</sup>, fitting the term-neonate double-gamma HRF<sup>44,69</sup>. A group average t-statistic map was generated using the 18 subjects' regression parameter maps. Regression parameter maps were used as subject-level response maps; the group-average t-statistic map was used as the group-level response map. The group-level response map was regressed onto each subject-level response map producing a spatial regression coefficient, constituting each subject's overall noxious-evoked response amplitude (Supplementary Figure 10 Step 1). The influence of HRF goodness-of-fit on noxious-evoked response amplitudes was assessed in Supplementary Information (Supplementary Figures 1 and 3).

To localise the noxious-evoked activity, we generated a thresholded group average activity map using group-level voxelwise GLM analysis in FSL's Randomise<sup>87</sup>. Statistical significance was assessed using permutation testing with 10,000 permutations, variance smoothing (6 mm FWHM kernel) due to limited degrees of freedom<sup>88</sup>, cluster-based thresholding with  $z=3.1$  ( $p=0.001$ ) cluster-defining threshold<sup>89</sup>, and a FWER-corrected cluster  $p$ -value of  $p=0.05$ . Regions of activity were identified using the probabilistic Harvard-Oxford Cortical Structural Atlas<sup>90</sup>.

To gain insight into the processes underlying the noxious-evoked activity, we assessed expression of several adult pain signature templates and Neurosynth meta-analysis association test map templates by performing whole-brain correlations between adult template maps and subject-level response maps (Supplementary Figure 10 Step 2). For each template,  $n=18$  correlation coefficients were generated, and group average template expression (average correlation) was assessed using two-tailed t-tests with statistical significance assessed non-parametrically in FSL's PALM<sup>87</sup> using 10,000 permutations.

The adult pain signatures tested were the Neurologic Pain Signature (NPS) and Social Rejection Pain signature, where the social rejection template was used as a negative control, as per the original NPS adult study<sup>37</sup>. Association test maps were used for all Neurosynth terms, as these maps display brain regions that are preferentially related to the term-of-interest. The primary Neurosynth term-of-interest was "pain"; "visual" was used as a Neurosynth negative control; a subset of pertinent pain dimension was assessed, including the sensory-discriminative term "nociceptive", the cognitive terms "arousal", "salience", and "attention", and the emotional term "unpleasant". Due to the whole-brain nature of the expression correlations and the default thresholded nature of all adult template maps included, we used the thresholded group average activity map generated from the neonates' noxious-evoked responses (thresholding performed in Randomise as described above) as the positive control. While the correlation between this thresholded noxious-evoked response map and the neonates' response maps is likely

inflated due to the circular analysis, the correlation strength of this positive control sets a useful upper limit reference.

Finally, inter-subject variability in noxious-evoked response amplitudes (regression parameters) and adult template correspondences (correlation coefficients) were assessed for all functional templates using two-tailed Pearson correlation tests with statistical significance assessed non-parametrically in PALM using 10,000 permutations.

### **Noxious stimulation imaging confounds**

In all analyses using noxious-evoked response, amplitudes were adjusted for (i) mean head motion: mean framewise displacement, (ii) stimulus-correlated head motion: multiple correlation coefficient between the predicted BOLD response (stimulus timeseries convolved with the HRF) and the 24 head motion timeseries (estimated during preprocessing), and (iii) CSF signal amplitude: the mean regression coefficient within the CSF ROI, intended to capture residual cardiac pulsatility. Details on ROI construction are provided in Supplementary Information (Supplementary Figure 8).

### **Resting-state network amplitudes**

To define a robust set of resting-state networks (RSNs), RSNs identified in the noxious stimulation paradigm dataset (n=18) were compared to those identified in a dHCP dataset previously produced as part of the dHCP<sup>38</sup> (Supplementary Figure 10 Step 3). Robust networks were defined as those replicated across datasets to ensure networks were not dataset-specific. This dHCP dataset included 242 healthy term-aged neonates: mean GA at birth = 38.6 weeks; mean PMA at scan = 40.4 weeks; 112 females<sup>38</sup>. The RSN analysis performed on our noxious stimulation paradigm dataset was matched to that of the dHCP dataset<sup>38,47</sup>. In brief, probabilistic functional mode (PFM) analysis using FSL's PROFUMO<sup>91,92</sup> was run with a pre-specified dimensionality of 25, using the term-neonate double-gamma HRF<sup>44,69</sup> as the temporal prior. PROFUMO's Bayesian model complexity penalties eliminated modes unsupported by the data, thus returning a number of group-level modes less than the pre-specified dimensionality. The data-determined dimensionality for the noxious stimulation paradigm dataset was 11, nine of which corresponded to the dHCP dataset resting-state networks assessed using spatial correlation followed by visual confirmation. Due to the larger sample size, the dHCP RSN maps had greater SNR and were thus used throughout our analyses as the nine RSN template maps.

These RSN template maps were spatially regressed onto each neonate's resting-state data using multiple regression, resulting in network timeseries. Timeseries amplitudes were quantified as the median absolute deviation (MAD), due to MAD's increased robustness to outliers compared to the more commonly used standard deviation (Supplementary Figure 10 Step 4). The association between network timeseries outliers and noxious-evoked response amplitudes was assessed in Supplementary Information (Supplementary Figures 2 and 3).

### **Resting-state imaging confounds**

In all analyses using RSN amplitudes, amplitudes were adjusted for (i) mean head motion: mean framewise displacement, (ii) CSF amplitude: timeseries MAD extracted using the CSF ROI, intended to capture residual cardiac pulsatility, and (iii) white matter amplitude: timeseries MAD extracted using the white matter ROI, intended to capture global signal amplitude. Details on ROI construction are provided in Supplementary Information (Supplementary Figure 8). These confounds were also directly tested for association with noxious-evoked response amplitudes.

## **Clinical variables**

Six clinical variables were tested for association with noxious-evoked response amplitudes: postmenstrual age (PMA), gestational age (GA), postnatal age (PNA), birth weight (BW), total brain volume (TBV), and sex (Table 3). Age variables are defined according to the American Academy of Paediatrics<sup>93</sup>, and TBV was calculated from neonates' structural MRI tissue segmentation outputs. Testing the clinical variables assessed whether associations between RSN amplitudes and noxious-evoked response amplitudes could be explained by these biologically interesting variables.

## **Predicting noxious-evoked response amplitudes**

For prediction analyses (Supplementary Figure 10 Step 5), the primary responses to be predicted were the neonates' overall noxious-evoked response amplitudes (Figure 1 scalar values). Three sets of predictors were tested for predictive capacity: nine RSN amplitudes, six clinical variables, and three resting-state imaging confounds. To further assess whether pain components of the overall noxious-evoked response amplitudes can themselves be predicted from resting-state data, we assessed RSN amplitude-based predictions for both the NPS and Neurosynth pain map response magnitudes. Adult pain signature response magnitudes were quantified using cosine similarity, which is equivalent to the Pearson correlation coefficient without mean-centring, thus retaining magnitude information.

For each set of predictors, a multivariate linear support vector regression (SVR) model was used to generate predictions using leave-one-out cross-validation (LOO-CV). The linear SVR model was fit using scikit-learn packages<sup>94</sup>. Noxious-evoked, NPS, and Neurosynth pain responses were all adjusted for the noxious-evoked response imaging confounds, and RSN amplitudes were adjusted for the resting-state imaging confounds using cross-validated confound regression (<https://github.com/lukassnoek/MVCA>)<sup>95</sup>. SVR parameters were: kernel=linear, loss=epsilon insensitive, epsilon=0.1, regularization=ridge, regularization strength={0.001, 0.01, 0.1, 1}. Regularization strength optimisation was performed using an initial LOO-CV grid search.

Prediction performance was assessed using root mean squared error (RMSE), sums-of-squares coefficient of determination ( $R^2$ ), and Spearman's rank correlation coefficient ( $R_{Sp}$ ). We performed one-tailed significance tests for these measures using permutation tests, running 1,000 permutations through the full prediction pipeline. The relationship between individual predictors and noxious-evoked response amplitudes was assessed in Supplementary Information (Supplementary Figure 4).

## **Part 2: Relating noxious-evoked response amplitude to white matter microstructure**

### **Structure-function analysis using an exploratory-confirmatory approach**

The neonates' noxious-evoked response amplitudes were assessed for structure-function associations by analysing white matter microstructure. Due to lack of research into the microstructural basis of noxious-evoked responses in healthy neonates, an exploratory analysis was required. However, due to the small sample size of the noxious stimulation paradigm dataset (n=17, Table 3), appropriate corrections for multiple testing would prohibit identification of true positives.

We thus adopted a two-armed two-dataset exploratory-confirmatory analysis approach. In the initial exploratory arm, we used a large age-matched dHCP sample to test a range of microstructural features to identify candidate white matter tracts and diffusion model parameters (Supplementary Figure 10 Step 6). Structure-function relationships identified here were used to formulate data-driven hypotheses. In the confirmatory arm, these hypotheses were subsequently tested for validation in the noxious stimulation paradigm dataset (Supplementary Figure 10 Step 7). Cross-dataset consistencies in structure-function associations constitute initial indirect external validation for the resting-state prediction model, as these consistencies rely on the predicted response amplitudes in the dHCP dataset being similar in nature to the true response amplitudes in the noxious stimulation paradigm dataset.

### **dHCP dataset sample selection**

Neonates were included in our dHCP sample if data were of reasonable quality and neonates were age-matched to our noxious stimulation paradigm dataset. The three data quality criteria were: (i) both fMRI and dMRI data passed dHCP QC pipelines<sup>47,82</sup>, (ii) both scan sessions completed fully, and (iii) the vertex of the cerebral cortex remained within the scan field of view for at least 95% of the scan session. The two age criteria were: (i) neonates were between 36–42 weeks for both GA and PMA, and (ii) neonates were scanned within the first 10 postnatal days. These criteria resulted in a sample of n=215 neonates. Key functional and diffusion acquisition parameters for this dHCP dataset are displayed in Table 4 to facilitate comparison with our noxious stimulation paradigm dataset.

### **dHCP dataset noxious-evoked response amplitudes**

The dHCP dataset does not include noxious stimulation paradigm data. To analyse structure-function relationships relevant to noxious-evoked responses, the dHCP resting-state data were mapped to noxious-evoked response amplitudes using the RSN amplitude-based SVR prediction model described above. This model was trained on the noxious stimulation paradigm dataset (n=18) using the nine confound-adjusted RSN amplitudes as predictors and the confound-adjusted noxious-evoked response amplitudes as responses. In our dHCP dataset (n=215), predictors and confounds were extracted in an identical manner to the noxious stimulation paradigm dataset analysis, and the RSN amplitudes were used to generate predicted noxious-evoked response amplitudes.

## White matter microstructural features

Our dHCP sample (n=215) was used to generate 16 bilateral white matter tracts using the “baby autoPtx” approach established as part of the dHCP dMRI preprocessing pipeline development<sup>35</sup>. In brief, FSL’s probabilistic multi-shell ball and zeppelins model<sup>96</sup> is fit, then probabilistic tractography using FSL’s PROBTRACKX<sup>97,98</sup> is run using pre-defined seed, target, and exclusion masks. At the time of analysis, 29 tracts were available, 13 unilateral and three bilateral. Unilateral tracts were fused to create bilateral tracts analogous to our bilateral resting-state networks, resulting in a total of 16 bilateral tracts: acoustic radiation, anterior thalamic radiation, cingulate gyrus part of the cingulum, parahippocampal part of the cingulum, corticospinal tract, forceps major, forceps minor, fornix, inferior fronto-occipital fasciculus, inferior longitudinal fasciculus, middle cerebellar peduncle, medial lemniscus, posterior thalamic radiation, superior longitudinal fasciculus, superior thalamic radiation, uncinata fasciculus. Normalised probability value results of each tract were group-averaged in standard space and thresholded at a probability of 0.01.

We used FSL’s DTIFIT to generate mean diffusivity (MD), fractional anisotropy (FA), and mean kurtosis (MK) parameter maps. We used the MD and FA maps from the b1000 shell, and MK maps from all three shells in both datasets. We thresholded each parameter map to remove noisy voxels with values outside the expected theoretical range, likely due to poor SNR or head motion: negative values for MD; values outside [0,1] for FA; values outside [0,3] for MK. Mean parameter values for each tract constituted the white matter microstructural features for our structure-function analyses. Comparisons of these microstructural features between the noxious stimulation paradigm and dHCP datasets is assessed in Supplementary Information (Supplementary Figure 6).

## Identifying nociception-related structure-function associations

### *Exploratory arm analyses:*

Using the dHCP sample (n=215), univariate correlations between predicted noxious-evoked response amplitudes and each microstructural feature was assessed using two-tailed Pearson correlations adjusted for three dMRI imaging confounds: mean head motion, number of noisy voxels outside expected theoretical ranges, and TBV. Adjustment for TBV mitigates macrostructural tissue density and partial volume effect confounds, which can bias dMRI microstructural parameters. Statistical significance was assessed using 10,000 permutations and FWER-corrected for multiple testing across all 48 tests (16 tracts x 3 parameters)<sup>99</sup>. While significant correlations are statistically valid, they are tentative due to the use of predicted noxious-evoked response amplitudes without a known ground truth.

Due to the presence of consistent structure-function correlation polarities across tracts identified in the dHCP dataset, variance across multiple tracts for a single dMRI parameter was pooled using principal component analysis (PCA). The first principal component across these tracts (e.g. MD PC1) was assessed for associations with noxious-evoked response amplitudes using two-tailed Pearson correlations, significance assessed using 10,000 permutations. In the dHCP dataset, these effect size and

statistical significance measures are biased due to circularity in explanatory variable selection<sup>39</sup>, but the bias is restricted to the exploratory arm analyses.

#### *Confirmatory arm analyses:*

The two hypotheses formulated in the dHCP dataset (see Results) were tested in the noxious stimulation paradigm dataset. First, the polarity of the Pearson correlation coefficient between noxious-evoked response amplitudes and individual tracts were qualitatively assessed. While similar correlation polarities alone are not strong evidence, when considered in combination with other elements of evidence, this correlation polarity information provides useful complementary insight. Second, the correlation between noxious-evoked response amplitudes and microstructural features of specific subsets of tracts was assessed using one-tailed Pearson correlation tests, the directionality of the tailed test hypothesised by the nature of the exploratory arm results. Statistical significance was assessed in PALM using 10,000 permutations. The effects of both global and local structure-function association effects observed in both the dHCP and noxious stimulation paradigm datasets were further assessed in Supplementary Information (Supplementary Figures 7-8).

#### **Data Availability**

Source data for figures 1-6 are provided with the paper. The data that support the findings of this study are available from the corresponding author upon reasonable request.

## **Declarations**

#### **Acknowledgements**

We are grateful for the provision of simultaneous multi-slice (multi-band) pulse sequence and reconstruction algorithms from the Centre for Magnetic Resonance Research, University of Minnesota. The dHCP resting-state network data were provided by the developing Human Connectome Project, KCL-Imperial-Oxford Consortium funded by the European Research Council under the European Union Seventh Framework Programme (FP/2007-2013) / ERC Grant Agreement no. [319456]. We are grateful to the families who generously supported this trial.

#### **Author Contributions**

LB conceived the idea for the study, analysed the data, interpreted the results, and wrote the paper. FM collected the data and revised the paper. SF provided technical assistance with the dHCP fMRI preprocessing pipeline, provided the dHCP resting-state network maps, and revised the paper. MA analysed the data and revised the paper. RM analysed the data and revised the paper. MB provided technical assistance with the dHCP dMRI preprocessing pipeline, provided the dHCP white matter tract maps, and revised the paper. RR interpreted the results and revised the paper. SJ designed the experiment, interpreted the results, and revised the paper. ED designed the experiment, interpreted the results, and

revised the paper. RS conceived the idea for the study, designed the experiment, interpreted the results, and wrote the paper.

## Competing Interests

The authors declare no competing interests.

## References

1. Carbajal, R. *et al.* Epidemiology and treatment of painful procedures in neonates in intensive care units. *JAMA* **300**, 60–70 (2008).
2. Lee, G. & Stevens, B. Neonatal and infant pain assessment. in *Oxford Textbook of Paediatric Pain* 353–369 (Oxford University Press, 2013).
3. Hartley, C. *et al.* The relationship between nociceptive brain activity, spinal reflex withdrawal and behaviour in newborn infants. *Scientific Reports* **5**, 12519 (2015).
4. Johnston, C. C. *et al.* Factors explaining lack of response to heel stick in preterm newborns. *J Obstet Gynecol Neonatal Nurs* **28**, 587–594 (1999).
5. Ranger, M., Johnston, C. C. & Anand, K. J. S. Current controversies regarding pain assessment in neonates. *Semin. Perinatol.* **31**, 283–288 (2007).
6. Verriotis, M. *et al.* Mapping Cortical Responses to Somatosensory Stimuli in Human Infants with Simultaneous Near-Infrared Spectroscopy and Event-Related Potential Recording. *eNeuro* **3**, (2016).
7. Hartley, C. *et al.* Nociceptive brain activity as a measure of analgesic efficacy in infants. *Sci Transl Med* **9**, (2017).
8. Verriotis, M. *et al.* Cortical activity evoked by inoculation needle prick in infants up to one-year old. *Pain* **156**, 222–230 (2015).
9. Magerl, W., Fuchs, P. N., Meyer, R. A. & Treede, R. D. Roles of capsaicin-insensitive nociceptors in cutaneous pain and secondary hyperalgesia. *Brain* **124**, 1754–1764 (2001).
10. Goksan, S. *et al.* fMRI reveals neural activity overlap between adult and infant pain. *Elife* **4**, (2015).
11. Iannetti, G. D., Baumgärtner, U., Tracey, I., Treede, R. D. & Magerl, W. Pinprick-evoked brain potentials: a novel tool to assess central sensitization of nociceptive pathways in humans. *J. Neurophysiol.* **110**, 1107–1116 (2013).
12. Slater, R. *et al.* Evoked potentials generated by noxious stimulation in the human infant brain. *Eur J Pain* **14**, 321–326 (2010).
13. Slater, R. *et al.* Cortical pain responses in human infants. *J. Neurosci.* **26**, 3662–3666 (2006).
14. Tracey, I. & Mantyh, P. W. The cerebral signature for pain perception and its modulation. *Neuron* **55**, 377–391 (2007).
15. Wiech, K. Deconstructing the sensation of pain: The influence of cognitive processes on pain perception. *Science* **354**, 584–587 (2016).

16. IASP. IASP Terminology - IASP. <https://www.iasp-pain.org/Education/Content.aspx?ItemNumber=1698> (2020).
17. Duff, E. *et al.* Inferring pain experience in infants using quantitative whole-brain functional MRI signatures: a cross-sectional, observational study. *The Lancet Digital Health* **2**, e458–e467 (2020).
18. Goksan, S. *et al.* The influence of the descending pain modulatory system on infant pain-related brain activity. *Elife* **7**, (2018).
19. Gibbins, S. *et al.* Validation of the Premature Infant Pain Profile-Revised (PIPP-R). *Early Human Development* **90**, 189–193 (2014).
20. Stevens, B., Johnston, C., Taddio, A., Gibbins, S. & Yamada, J. The premature infant pain profile: evaluation 13 years after development. *Clin J Pain* **26**, 813–830 (2010).
21. Stevens, B. J. *et al.* The premature infant pain profile-revised (PIPP-R): initial validation and feasibility. *Clin J Pain* **30**, 238–243 (2014).
22. McDowell, I. The Theoretical and Technical Foundations of Health Measurement. in *Measuring Health: A guide to rating scales and questionnaires* (Oxford University Press, 2006).
23. Worley, A., Fabrizi, L., Boyd, S. & Slater, R. Multi-modal pain measurements in infants. *J Neurosci Methods* **205**, 252–257 (2012).
24. Vaart, M. *et al.* Multimodal pain assessment improves discrimination between noxious and non-noxious stimuli in infants. *Paediatric and Neonatal Pain* **1**, 21–30 (2019).
25. Yarkoni, T., Poldrack, R. A., Nichols, T. E., Van Essen, D. C. & Wager, T. D. Large-scale automated synthesis of human functional neuroimaging data. *Nat Methods* **8**, 665–670 (2011).
26. Cole, M. W., Bassett, D. S., Power, J. D., Braver, T. S. & Petersen, S. E. Intrinsic and task-evoked network architectures of the human brain. *Neuron* **83**, 238–251 (2014).
27. Smith, S. M. *et al.* Correspondence of the brain's functional architecture during activation and rest. *Proc. Natl. Acad. Sci. U.S.A.* **106**, 13040–13045 (2009).
28. Finn, E. S. *et al.* Functional connectome fingerprinting: identifying individuals using patterns of brain connectivity. *Nat. Neurosci.* **18**, 1664–1671 (2015).
29. Tavor, I. *et al.* Task-free MRI predicts individual differences in brain activity during task performance. *Science* **352**, 216–220 (2016).
30. Parker Jones, O., Voets, N. L., Adcock, J. E., Stacey, R. & Jbabdi, S. Resting connectivity predicts task activation in pre-surgical populations. *Neuroimage Clin* **13**, 378–385 (2017).
31. Spisak, T. *et al.* Pain-free resting-state functional brain connectivity predicts individual pain sensitivity. *Nature Communications* **11**, 187 (2020).
32. Doria, V. *et al.* Emergence of resting state networks in the preterm human brain. *Proc. Natl. Acad. Sci. U.S.A.* **107**, 20015–20020 (2010).
33. Fransson, P. *et al.* Resting-state networks in the infant brain. *Proc. Natl. Acad. Sci. U.S.A.* **104**, 15531–15536 (2007).

34. Jones, L. *et al.* Nociceptive Cortical Activity Is Dissociated from Nociceptive Behavior in Newborn Human Infants under Stress. *Curr. Biol.* **27**, 3846-3851.e3 (2017).
35. Bastiani, M. *et al.* Automated processing pipeline for neonatal diffusion MRI in the developing Human Connectome Project. *Neuroimage* **185**, 750–763 (2019).
36. Apkarian, A. V., Bushnell, M. C., Treede, R.-D. & Zubieta, J.-K. Human brain mechanisms of pain perception and regulation in health and disease. *Eur J Pain* **9**, 463–484 (2005).
37. Wager, T. D. *et al.* An fMRI-based neurologic signature of physical pain. *N. Engl. J. Med.* **368**, 1388–1397 (2013).
38. Fitzgibbon, S. *et al.* The developing Human Connectome Project automated functional processing framework for neonates. *OHBM* (2018).
39. Kriegeskorte, N., Simmons, W. K., Bellgowan, P. S. F. & Baker, C. I. Circular analysis in systems neuroscience: the dangers of double dipping. *Nat. Neurosci.* **12**, 535–540 (2009).
40. Slater, R., Cantarella, A., Franck, L., Meek, J. & Fitzgerald, M. How well do clinical pain assessment tools reflect pain in infants? *PLoS Med.* **5**, e129 (2008).
41. Dubois, J. *et al.* The early development of brain white matter: a review of imaging studies in fetuses, newborns and infants. *Neuroscience* **276**, 48–71 (2014).
42. Ouyang, M., Dubois, J., Yu, Q., Mukherjee, P. & Huang, H. Delineation of early brain development from fetuses to infants with diffusion MRI and beyond. *Neuroimage* **185**, 836–850 (2019).
43. Lenz, F. A., Casey, K. L., Jones, E. G. & Willis, W. D. *The Human Pain System: Experimental and Clinical Perspectives.* (Cambridge University Press, 2010). doi:10.1017/CBO9780511770579.
44. Arichi, T. *et al.* Development of BOLD signal hemodynamic responses in the human brain. *Neuroimage* **63**, 663–673 (2012).
45. Kozberg, M. & Hillman, E. Neurovascular coupling and energy metabolism in the developing brain. *Prog. Brain Res.* **225**, 213–242 (2016).
46. Goense, J., Bohraus, Y. & Logothetis, N. K. fMRI at High Spatial Resolution: Implications for BOLD-Models. *Front. Comput. Neurosci.* **10**, (2016).
47. Fitzgibbon, S. P. *et al.* The developing Human Connectome Project (dHCP) automated resting-state functional processing framework for newborn infants. *Neuroimage* **223**, 117303 (2020).
48. Smyser, C. D. *et al.* Longitudinal analysis of neural network development in preterm infants. *Cereb. Cortex* **20**, 2852–2862 (2010).
49. Cao, M. *et al.* Early Development of Functional Network Segregation Revealed by Connectomic Analysis of the Preterm Human Brain. *Cereb. Cortex* **27**, 1949–1963 (2017).
50. Dubois, J. *et al.* Asynchrony of the early maturation of white matter bundles in healthy infants: quantitative landmarks revealed noninvasively by diffusion tensor imaging. *Hum Brain Mapp* **29**, 14–27 (2008).
51. Tsuchida, T. N. *et al.* American clinical neurophysiology society standardized EEG terminology and categorization for the description of continuous EEG monitoring in neonates: report of the American

- Clinical Neurophysiology Society critical care monitoring committee. *J Clin Neurophysiol* **30**, 161–173 (2013).
52. Bzdok, D. *et al.* Formal Models of the Network Co-occurrence Underlying Mental Operations. *PLoS Comput. Biol.* **12**, e1004994 (2016).
  53. Arichi, T. *et al.* Somatosensory cortical activation identified by functional MRI in preterm and term infants. *Neuroimage* **49**, 2063–2071 (2010).
  54. Anderson, A. W. *et al.* Neonatal auditory activation detected by functional magnetic resonance imaging. *Magn Reson Imaging* **19**, 1–5 (2001).
  55. Deen, B. *et al.* Organization of high-level visual cortex in human infants. *Nat Commun* **8**, 13995 (2017).
  56. Colonnese, M. & Khazipov, R. Spontaneous activity in developing sensory circuits: Implications for resting state fMRI. *NeuroImage* **62**, 2212–2221 (2012).
  57. Edwards, L. J., Pine, K. J., Ellerbrock, I., Weiskopf, N. & Mohammadi, S. NODDI-DTI: Estimating Neurite Orientation and Dispersion Parameters from a Diffusion Tensor in Healthy White Matter. *Front. Neurosci.* **11**, (2017).
  58. Zhang, H., Schneider, T., Wheeler-Kingshott, C. A. & Alexander, D. C. NODDI: practical in vivo neurite orientation dispersion and density imaging of the human brain. *Neuroimage* **61**, 1000–1016 (2012).
  59. Nielsen, C. S., Staud, R. & Price, D. D. Individual differences in pain sensitivity: measurement, causation, and consequences. *J Pain* **10**, 231–237 (2009).
  60. Doesburg, S. M. *et al.* Neonatal pain-related stress, functional cortical activity and visual-perceptual abilities in school-age children born at extremely low gestational age. *Pain* **154**, 1946–1952 (2013).
  61. Vinall, J. *et al.* Invasive procedures in preterm children: brain and cognitive development at school age. *Pediatrics* **133**, 412–421 (2014).
  62. Denk, F., McMahon, S. B. & Tracey, I. Pain vulnerability: a neurobiological perspective. *Nat. Neurosci.* **17**, 192–200 (2014).
  63. Grunau, R. E., Holsti, L. & Peters, J. W. B. Long-term consequences of pain in human neonates. *Semin Fetal Neonatal Med* **11**, 268–275 (2006).
  64. Goksan, S. *et al.* Optimal echo time for functional MRI of the infant brain identified in response to noxious stimulation. *Magn Reson Med* **78**, 625–631 (2017).
  65. Moeller, S. *et al.* Multiband multislice GE-EPI at 7 tesla, with 16-fold acceleration using partial parallel imaging with application to high spatial and temporal whole-brain fMRI. *Magn Reson Med* **63**, 1144–1153 (2010).
  66. Xu, J. *et al.* Evaluation of slice accelerations using multiband echo planar imaging at 3 T. *Neuroimage* **83**, 991–1001 (2013).
  67. Makropoulos, A. *et al.* Automatic whole brain MRI segmentation of the developing neonatal brain. *IEEE Trans Med Imaging* **33**, 1818–1831 (2014).

68. Makropoulos, A. *et al.* The developing human connectome project: A minimal processing pipeline for neonatal cortical surface reconstruction. *Neuroimage* **173**, 88–112 (2018).
69. Baxter, L. *et al.* Optimising neonatal fMRI data analysis: Design and validation of an extended dHCP preprocessing pipeline to characterise noxious-evoked brain activity in infants. *Neuroimage* **186**, 286–300 (2019).
70. Andersson, J. L. R. & Sotiropoulos, S. N. An integrated approach to correction for off-resonance effects and subject movement in diffusion MR imaging. *Neuroimage* **125**, 1063–1078 (2016).
71. Andersson, J. L. R. & Sotiropoulos, S. N. Non-parametric representation and prediction of single- and multi-shell diffusion-weighted MRI data using Gaussian processes. *Neuroimage* **122**, 166–176 (2015).
72. Andersson, J. L. R. *et al.* Towards a comprehensive framework for movement and distortion correction of diffusion MR images: Within volume movement. *Neuroimage* **152**, 450–466 (2017).
73. Andersson, J. L. R., Graham, M. S., Drobnjak, I., Zhang, H. & Campbell, J. Susceptibility-induced distortion that varies due to motion: Correction in diffusion MR without acquiring additional data. *Neuroimage* **171**, 277–295 (2018).
74. Griffanti, L. *et al.* ICA-based artefact removal and accelerated fMRI acquisition for improved resting state network imaging. *Neuroimage* **95**, 232–247 (2014).
75. Salimi-Khorshidi, G. *et al.* Automatic denoising of functional MRI data: combining independent component analysis and hierarchical fusion of classifiers. *Neuroimage* **90**, 449–468 (2014).
76. Smith, S. M. & Brady, J. M. SUSAN—A New Approach to Low Level Image Processing. *International Journal of Computer Vision* **23**, 45–78 (1997).
77. Greve, D. N. & Fischl, B. Accurate and robust brain image alignment using boundary-based registration. *Neuroimage* **48**, 63–72 (2009).
78. Jenkinson, M., Bannister, P., Brady, M. & Smith, S. Improved optimization for the robust and accurate linear registration and motion correction of brain images. *Neuroimage* **17**, 825–841 (2002).
79. Jenkinson, M. & Smith, S. A global optimisation method for robust affine registration of brain images. *Med Image Anal* **5**, 143–156 (2001).
80. Schuh, A. *et al.* Unbiased construction of a temporally consistent morphological atlas of neonatal brain development. *bioRxiv* 251512 (2018) doi:10.1101/251512.
81. Avants, B. B., Epstein, C. L., Grossman, M. & Gee, J. C. Symmetric diffeomorphic image registration with cross-correlation: evaluating automated labeling of elderly and neurodegenerative brain. *Med Image Anal* **12**, 26–41 (2008).
82. Bastiani, M. *et al.* Automated quality control for within and between studies diffusion MRI data using a non-parametric framework for movement and distortion correction. *Neuroimage* **184**, 801–812 (2019).
83. Andersson, J. L. R., Skare, S. & Ashburner, J. How to correct susceptibility distortions in spin-echo echo-planar images: application to diffusion tensor imaging. *Neuroimage* **20**, 870–888 (2003).

84. Smith, S. M. *et al.* Advances in functional and structural MR image analysis and implementation as FSL. *Neuroimage* **23 Suppl 1**, S208-219 (2004).
85. Andersson, J. L. R., Graham, M. S., Zsoldos, E. & Sotiropoulos, S. N. Incorporating outlier detection and replacement into a non-parametric framework for movement and distortion correction of diffusion MR images. *Neuroimage* **141**, 556–572 (2016).
86. Jenkinson, M., Beckmann, C. F., Behrens, T. E. J., Woolrich, M. W. & Smith, S. M. FSL. *NeuroImage* **62**, 782–790 (2012).
87. Winkler, A. M., Ridgway, G. R., Webster, M. A., Smith, S. M. & Nichols, T. E. Permutation inference for the general linear model. *Neuroimage* **92**, 381–397 (2014).
88. Holmes, A. P., Blair, R. C., Watson, J. D. & Ford, I. Nonparametric analysis of statistic images from functional mapping experiments. *J. Cereb. Blood Flow Metab.* **16**, 7–22 (1996).
89. Woo, C.-W., Krishnan, A. & Wager, T. D. Cluster-extent based thresholding in fMRI analyses: pitfalls and recommendations. *Neuroimage* **91**, 412–419 (2014).
90. Desikan, R. S. *et al.* An automated labeling system for subdividing the human cerebral cortex on MRI scans into gyral based regions of interest. *Neuroimage* **31**, 968–980 (2006).
91. Harrison, S. J. *et al.* Modelling subject variability in the spatial and temporal characteristics of functional modes. *NeuroImage* **222**, 117226 (2020).
92. Harrison, S. J. *et al.* Large-scale probabilistic functional modes from resting state fMRI. *Neuroimage* **109**, 217–231 (2015).
93. Engle, W. A. & American Academy of Pediatrics Committee on Fetus and Newborn. Age terminology during the perinatal period. *Pediatrics* **114**, 1362–1364 (2004).
94. Pedregosa, F. *et al.* Scikit-learn: Machine Learning in Python. *Journal of Machine Learning Research* **12**, 2825–2830 (2011).
95. Snoek, L., Miletic, S. & Scholte, H. S. How to control for confounds in decoding analyses of neuroimaging data. *Neuroimage* **184**, 741–760 (2019).
96. Sotiropoulos, S. N. *et al.* Fusion in diffusion MRI for improved fibre orientation estimation: An application to the 3T and 7T data of the Human Connectome Project. *Neuroimage* **134**, 396–409 (2016).
97. Behrens, T. E. J., Berg, H. J., Jbabdi, S., Rushworth, M. F. S. & Woolrich, M. W. Probabilistic diffusion tractography with multiple fibre orientations: What can we gain? *Neuroimage* **34**, 144–155 (2007).
98. Behrens, T. E. J. *et al.* Characterization and propagation of uncertainty in diffusion-weighted MR imaging. *Magn Reson Med* **50**, 1077–1088 (2003).
99. Winkler, A. M. *et al.* Non-parametric combination and related permutation tests for neuroimaging. *Hum Brain Mapp* **37**, 1486–1511 (2016).

## Tables

**Table 1: Noxious-evoked responses are pain-relevant signals.**

|                    | Noxious-evoked | Visual       | Pain           | Nociceptive    | Attention    |
|--------------------|----------------|--------------|----------------|----------------|--------------|
| <b>T-test</b>      | 4.68* (0.0007) | -0.51 (0.62) | 3.85* (0.0022) | 4.34* (0.0013) | 1.88 (0.078) |
| <b>Correlation</b> | 0.88* (0.0001) | 0.18 (0.47)  | 0.89* (0.0001) | 0.87* (0.0001) | 0.28 (0.26)  |
|                    | Unpleasant     | Saliience    | Arousal        | NPS            | Social       |
| <b>T-test</b>      | 0.49 (0.66)    | -0.15 (0.89) | -0.34 (0.76)   | 3.71* (0.0016) | 0.58 (0.56)  |
| <b>Correlation</b> | -0.33 (0.18)   | -0.11 (0.66) | -0.32 (0.19)   | 0.77* (0.0002) | 0.36 (0.14)  |

T-test results assess the group average presence or absence of template expression within the neonates' (n=18) noxious-evoked response maps. T-statistics and p-values are presented for each template. Correlation results assess the correspondence between the inter-individual variability in overall noxious-evoked response amplitudes and the correspondence between neonates' noxious-evoked response maps and each template. Pearson correlation coefficients and p-values are presented for each template. P-values are presented in parentheses. \* = statistically significant.

**Table 2: Noxious-evoked response amplitude prediction performance.**

| Predictors                | Responses       | R <sup>2</sup> | RMSE           | R <sub>Sp</sub> |
|---------------------------|-----------------|----------------|----------------|-----------------|
| <b>Resting state</b>      | Overall         | 0.62* (0.003)  | 1.57* (0.003)  | 0.79* (0.001)   |
|                           | Neurosynth pain | 0.46* (0.006)  | 0.15* (0.006)  | 0.65* (0.01)    |
|                           | NPS             | 0.42* (0.013)  | 0.025* (0.013) | 0.62* (0.014)   |
| <b>Clinical variables</b> | Overall         | 0.11 (0.25)    | 2.42 (0.25)    | 0.36 (0.19)     |
| <b>Confounds</b>          | Overall         | 0.081 (0.56)   | 2.46 (0.56)    | 0.14 (0.44)     |

Each row contains results for a specific set of predictors and responses. Each results column contains a prediction performance metric: R<sup>2</sup> = coefficient of determination (sums-of-squares formulation); RMSE = root mean squared error; R<sub>Sp</sub> = Spearman's rank correlation coefficient. P-values are presented in parentheses. \* = statistically significant.

**Table 3: Demographic details of the 18-neonate noxious stimulation paradigm dataset.**

| Neonate | PMA<br>(weeks) | GA<br>(weeks) | PNA<br>(days) | BW<br>(grams) | TBV<br>(mm <sup>3</sup> ) | Sex |
|---------|----------------|---------------|---------------|---------------|---------------------------|-----|
| 1       | 40.6           | 40.3          | 2             | 3,880         | 283,685                   | M   |
| 2       | 37.4           | 37.1          | 2             | 4,570         | 276,222                   | M   |
| 3       | 35.9           | 35.3          | 4             | 1,910         | 212,410                   | F   |
| 4       | 35.9           | 35.6          | 2             | 3,180         | 284,623                   | M   |
| 5       | 38.3           | 38            | 2             | 3,400         | 309,632                   | M   |
| 6       | 38             | 37.3          | 4             | 3,410         | 306,530                   | F   |
| 7       | 39.6           | 39.3          | 2             | 3,250         | 301,086                   | F   |
| 8       | 36.4           | 36            | 3             | 3,510         | 260,268                   | F   |
| 9       | 38             | 37.9          | 1             | 2,490         | 221,792                   | M   |
| 10      | 40.7           | 40.6          | 1             | 4,300         | 346,861                   | M   |
| 11      | 40.4           | 40.1          | 2             | 4,040         | 356,454                   | M   |
| 12      | 39.3           | 39            | 2             | 3,775         | 300,094                   | F   |
| 13      | 38.9           | 38.6          | 2             | 2,950         | 286,714                   | F   |
| 14*     | 41.7           | 41.4          | 2             | 3,400         | 297,004                   | M   |
| 15      | 40.4           | 39            | 10            | 3,750         | 416,904                   | F   |
| 16      | 38.3           | 38            | 2             | 2,780         | 247,199                   | M   |
| 17      | 37.4           | 36.4          | 7             | 2,235         | 257,069                   | F   |
| 18      | 39             | 38.9          | 1             | 3,350         | 252,271                   | M   |
| m       | 38.7           | 38.3          | 2.8           | 3,343.3       | 289,823.2                 | --- |
| s       | 1.7            | 1.8           | 2.3           | 690.4         | 49,020.8                  | --- |

Neonates are ordered as displayed in Figure 1 i.e. neonate 18 had largest response amplitude. PMA = postmenstrual age; GA = gestational age; PNA = postnatal age; BW = birth weight; TBV = total brain volume; m = mean; s = standard deviation. \* = excluded from structure-function association analyses due to incomplete dMRI data.

**Table 4: Comparison of key data acquisition parameters between the noxious stimulation paradigm (local) dataset and dHCP dataset for resting-state fMRI and dMRI data.**

|               | Parameter                         | Local dataset      | dHCP dataset       |
|---------------|-----------------------------------|--------------------|--------------------|
| Scanner       | Model                             | Siemens Prisma     | Philips Achieva    |
|               | Field strength                    | 3T                 | 3T                 |
| Head coil     | Channel density                   | 32-channel         | 32-channel         |
|               | Size                              | adult              | neonatal           |
| Resting-state | Echo time, TE (ms)                | 50                 | 38                 |
|               | Repetition time, TR (ms)          | 1300               | 392                |
|               | Multiband acceleration factor, MB | 4                  | 9                  |
|               | Voxel size, isotropic (mm)        | 2                  | 2.15               |
| Diffusion     | Number of volumes                 | 500                | 2300               |
|               | Echo time, TE (ms)                | 73                 | 90                 |
|               | Repetition time, TR (ms)          | 2900               | 3800               |
|               | Multiband acceleration factor     | 3                  | 4                  |
|               | Voxel size, isotropic (mm)        | 1.75               | 1.5                |
|               | Number of volumes                 | 163                | 300                |
|               | b-values (s/mm <sup>2</sup> )     | 0, 500, 1000, 2000 | 0, 400, 1000, 2600 |
|               | Number of volumes/directions      | 20, 23, 50, 70     | 20, 64, 88, 128    |
|               | Gradient duration, d (ms)         | 12.5               | 14                 |
|               | Gradient separation, D (ms)       | 35.5               | 42.5               |

## Figures

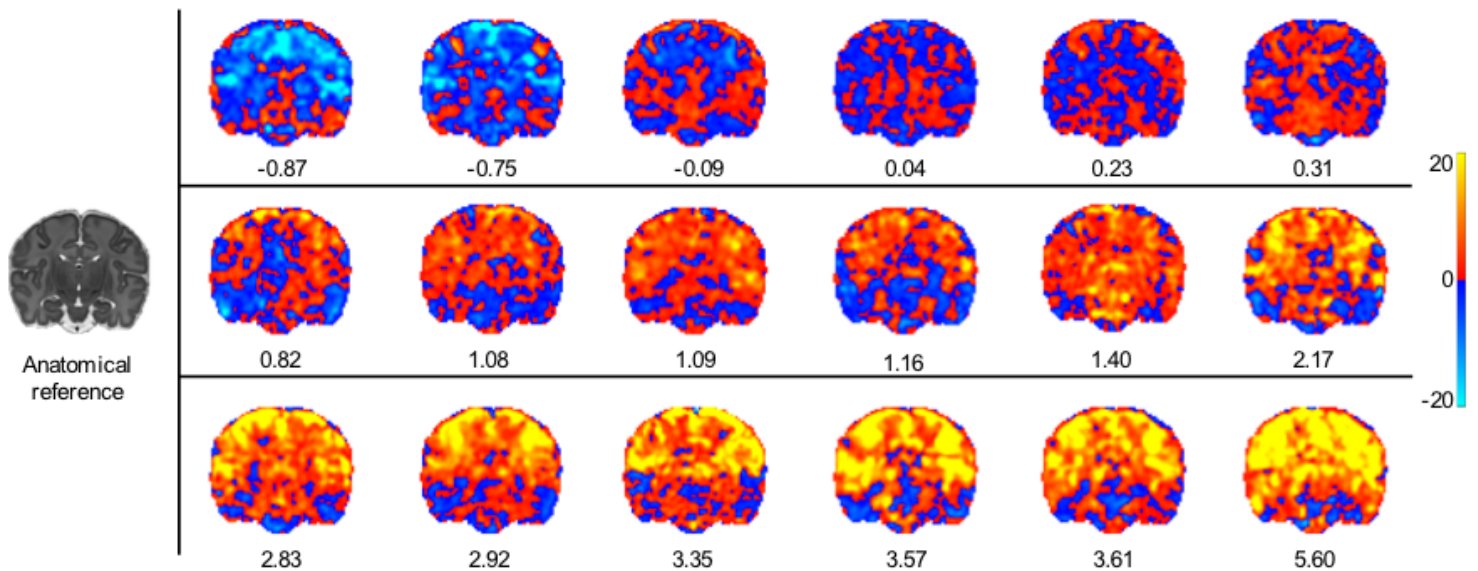


**Figure 1**

Noxious-evoked response amplitudes. A noxious-evoked response BOLD activity map is presented for each neonate (n=18) and ordered according to the overall response amplitude. The maps are general linear model regression parameter maps. The anatomical reference (left) provides structural detail for orientation. All maps are displayed at this slice position to maximally emphasise the range of individual

variability in response amplitudes. Unthresholded maps are used for visualisation to demonstrate the range of evoked response amplitudes from negative to negligible to positive amplitudes, without introducing the issues inherent to application of arbitrary thresholds. The scalar value presented below each map is a summary measure that represents the overall noxious-evoked response amplitude relative to the group average.

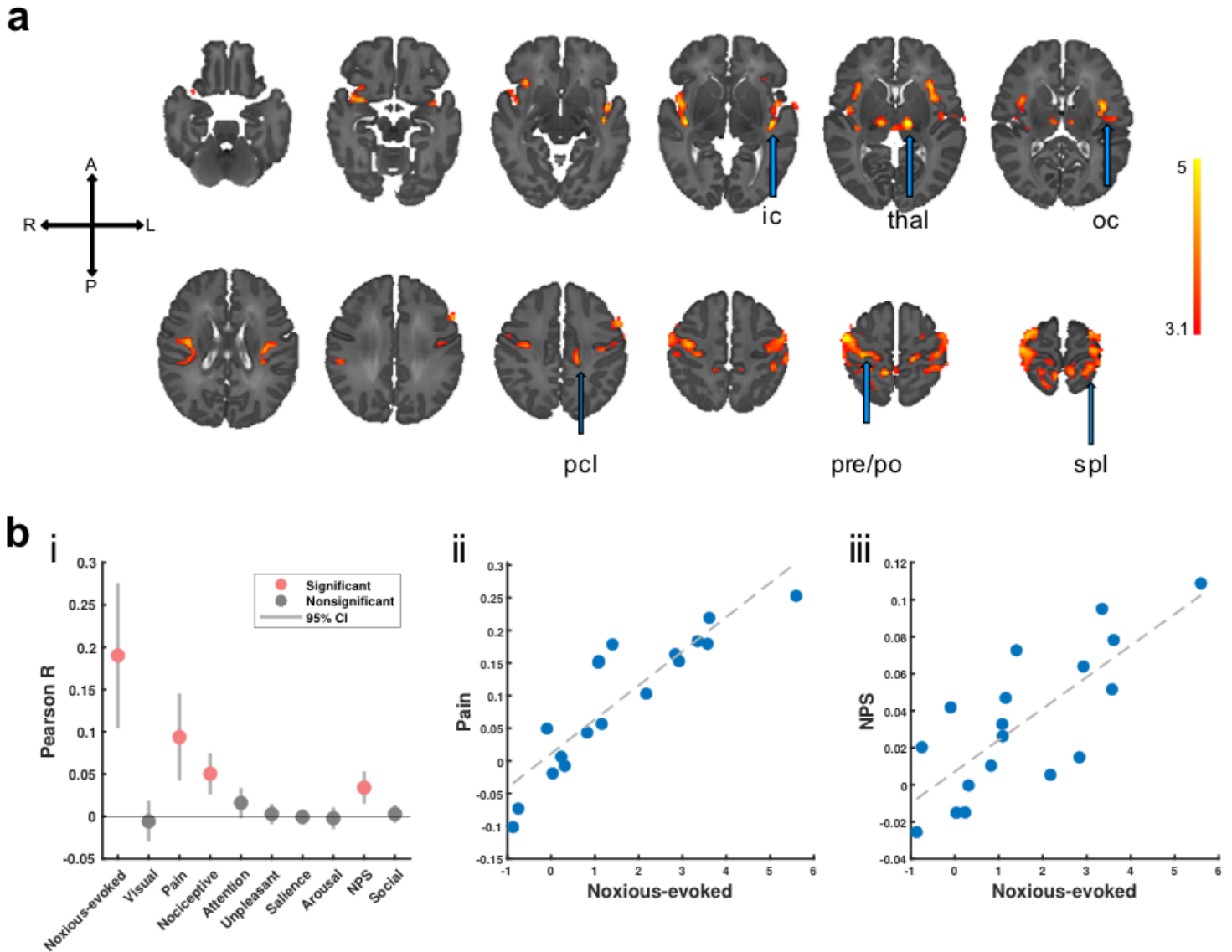


**Figure 2**

Noxious-evoked responses are pain-relevant signals. a. The thresholded group average noxious-evoked map displays t-statistics in statistically significant clusters. Activity is localised to regions classically considered part of the adult nociceptive pain system, including the pre- and post-central gyri (pre/po), paracentral and superior parietal lobules (pcl and spl), opercular and insular cortices (oc and ic), and thalamus (thal). b. i.: For each infant, expression of functional templates (x-axis) is assessed as whole-brain Pearson correlations between the template and neonates' noxious-evoked response maps (y-axis). Group average template expression was assessed using two-tailed t-tests (n=18). Grey and red dots represent the group mean correlation coefficient, with grey bars displaying 95% confidence intervals (CI).

The thresholded noxious-evoked map (displayed in part a) is the positive control. Visual is the Neurosynth negative control, and Social Rejection Pain is the pain signature negative control. The Neurologic Pain Signature (NPS) and Neurosynth Pain and Nociceptive templates were significantly expressed in this group of neonates, while none of the negative controls or other Neurosynth templates were significantly expressed. ii-iii.: Using two-tailed Pearson correlation tests to assess inter-subject variability in noxious-evoked responses, strong associations exist between the overall noxious-evoked response amplitudes (regression parameters) and both NPS and Neurosynth Pain correspondences (correlation coefficients). The dashed grey line is the least squares fit. The stronger the neonatal BOLD response amplitude to the noxious stimulus, the closer the correspondence with both adult pain signatures. T-test and correlation test results for all templates are summarised in Table 1.

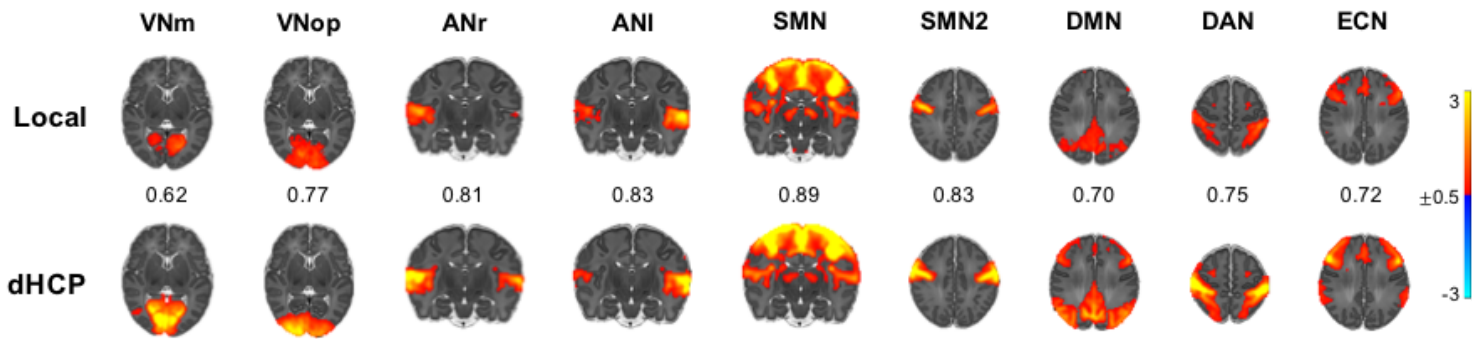


**Figure 3**

Nine resting-state networks replicated across two independent datasets. Each resting-state network map is a thresholded group-level probabilistic functional mode (PFM) map identified in the locally collected noxious stimulation paradigm dataset (n=18) (top row, Local) and the age-matched dHCP dataset (n=242) (bottom row, dHCP). These PFM posterior probability maps are thresholded to highlight qualitative correspondence. The scalar value shown between matched maps is the spatial Pearson correlation coefficient between unthresholded maps highlighting quantitative correspondence.

Abbreviations: VNm = medial visual network; VNop = occipital pole visual network; ANr = right auditory network; ANI = left auditory network; SMN = somatomotor network; DMN = default mode network; DAN = dorsal attention network; ECN = executive control network.

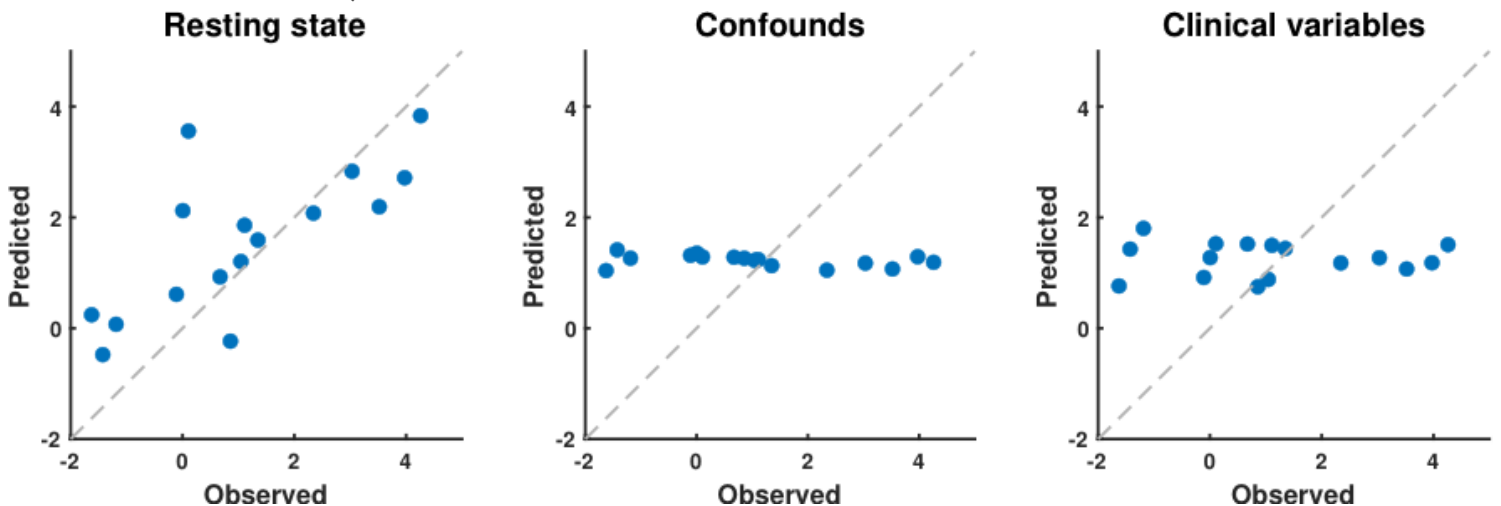


**Figure 4**

Predicting noxious-evoked response amplitudes from non-noxious data. For all plots, each blue dot represents an out-of-sample cross-validated prediction for a single neonate ( $n=18$ ), and the dashed grey line is the  $y=x$  line along which perfect predictions would lie. The x-axis is the observed noxious-evoked response amplitude (after cross-validated confound regression), and the y-axis is the predicted noxious-evoked response amplitude. Predictions were generated based on three sets of predictors: (left) the resting-state network amplitudes; (middle) resting-state imaging confounds, which included head motion, CSF amplitude, and white matter amplitude; and (right) clinical variables, which included age (gestational, postmenstrual, and postnatal), birth weight, total brain volume, and sex.

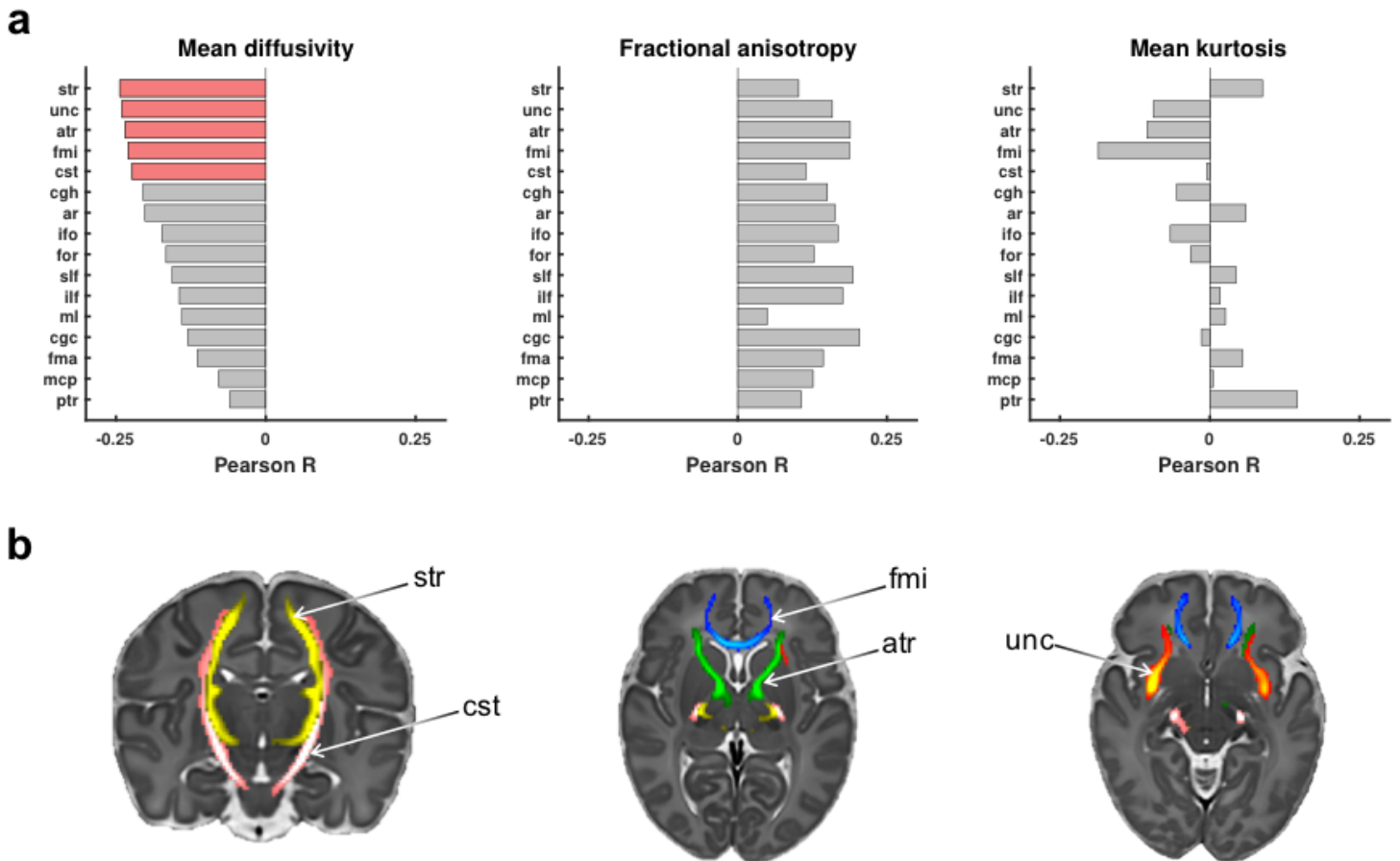


**Figure 5**

Exploration of structure-function associations in the dHCP dataset. The structural feature per white matter tract is the voxelwise mean diffusion parameter: mean diffusivity, fractional anisotropy, and mean kurtosis. The functional feature is the predicted noxious-evoked response amplitude, generated using the resting-state prediction model. a. The three plots display the Pearson correlation coefficients (x-axis) between response amplitudes and diffusion parameters for all 16 white matter tracts (y-axis). The white matter tracts are ordered according to the mean diffusivity correlation coefficients for which statistically significant results were found (red). Statistical significance is FWER-corrected for multiple testing across

all 48 Pearson correlation tests. b. Maps displaying the five bilateral white matter tracts statistically significantly related to predicted noxious-evoked response amplitudes. Abbreviations: ar = acoustic radiation; atr = anterior thalamic radiation; cgc = cingulate gyrus part of the cingulum; cgh = parahippocampal part of the cingulum; cst = corticospinal tract; fma = forceps major; fmi = forceps minor; for = fornix; ifo = inferior fronto-occipital fasciculus; ilf = inferior longitudinal fasciculus; mcp = middle cerebellar peduncle; ml = medial lemniscus; ptr = posterior thalamic radiation; slf = superior longitudinal fasciculus; str = superior thalamic radiation; unc = uncinate fasciculus.

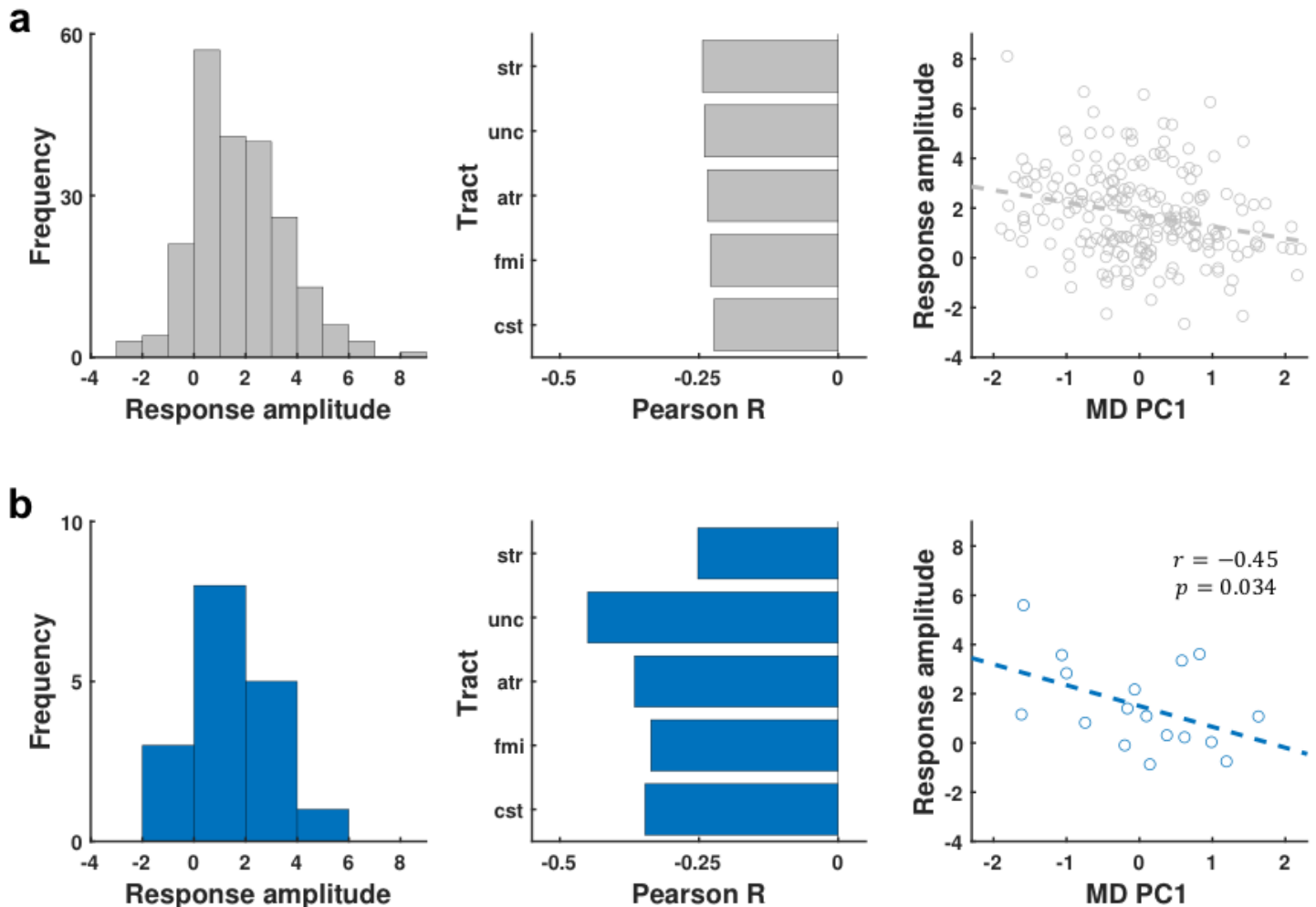


**Figure 6**

Confirmation of negative associations between noxious-evoked response amplitudes and white matter mean diffusivities in the noxious stimulation paradigm dataset. a. Results using predicted responses in dHCP dataset. b. Results using observed responses in noxious stimulation paradigm dataset. a and b. Left: histograms display the frequency distributions of the noxious-evoked response amplitudes. Middle: bar plots displaying the Pearson correlation coefficients between noxious-evoked response amplitudes and MD for the five white matter tracts identified in the exploratory arm analysis (Figure 5). Right: scatter plots displaying the negative correlation between noxious-evoked response amplitudes (y-axis) and MD PC 1 (x-axis). These cross-dataset consistencies confirm the exploratory arm findings and establish initial validation for the underlying resting-state prediction model. Abbreviations: atr = anterior thalamic

radiation; cst = corticospinal tract; fmi = forceps minor; str = superior thalamic radiation; unc = uncinata fasciculus; MD PC1 = mean diffusivity principal component 1; r = Pearson correlation coefficient; p = p-value associated with r.

## Supplementary Files

This is a list of supplementary files associated with this preprint. Click to download.

- [supplementaryinformationclean.pdf](#)